Rapid identification of micro and nanoplastics by line scan Raman micro-spectroscopy

Qingyi Wu [a,b], Dongyang Xiao [c], Nan Wang [c], Francesco Masia [d], Wolfgang Langbein [e,**], Bei Li [a,b,*]

[a] State Key Laboratory of Applied Optics, Changchun Institute of Optics, Fine Mechanics and Physics, Changchun, 130033, China
[b] University of Chinese Academy of Sciences, Beijing, 100049, China
[c] Hooke Instruments, Changchun, 130033, China
[d] School of Biosciences, Cardiff University, Cardiff, CF10 3AX, UK
[e] School of Physics and Astronomy, Cardiff University, Cardiff, CF24 3AA, UK

ABSTRACT

Microplastic pollution has become an environmental problem that cannot be ignored in our society. Raman spectroscopy technology has been widely used in the field of microplastics detection due to its non-contact, non-destructive chemical specificity. Traditional point confocal Raman micro-spectroscopy technology uses single-point detection, resulting in long measurement times to scan the large areas of interest of typical samples. In this paper, we present a line scan confocal Raman micro-spectroscopy tool for fast detection and identification of microplastic particles. We show size and composition identification of particles and imaging over large areas. Compared with point confocal Raman imaging, the line scan confocal Raman technology increases the imaging speed by 1–2 orders of magnitude.

1. Introduction

Microplastics are plastic particles less than 5 mm in size [1], and nanoplastics are below 1 μm in size [2] - both are resulting from the degradation of plastics, in the natural environment or by human activities. Despite the small size, their occurrence in the environment has become a concern as they are widespread due to the ubiquitous use of plastics in human society, of which a fraction is left in the natural world, and not recovered for recycling. This may have significant effects on the health of natural habitats and humans. If microplastics in the natural environment are accidently ingested by organisms, they can block vital functions and cause disease or death. In addition, various pollutants adsorbed on the surface of the microplastics can accumulate in the organisms and cause ecological hazards [3–6]. Therefore, it is of great significance to be able to detect and identify microplastics. Measuring the abundance, shape, size, and chemical composition of microplastics can enable the evaluation of its hazards.

A range of detection technology for microplastics has been reported in the literature. Visual inspection [7–9], including fluorescent labeling [10,11] to increase selectivity, can provide morphological information,

but cannot identify the chemical composition. Gas chromatography-mass spectrometry [12–15] provides chemical information but is a contact and destructive method. Fourier transform infrared spectroscopy [16–20], measuring vibrational resonances for chemical fingerprinting, has, due to the longer interrogating wavelength, a spatial resolution in the 10 μm range, and has difficulties identifying particles smaller than 5 μm. Raman spectroscopy is a vibrational spectroscopy technique based on inelastic scattering of light, in which the frequency shift identifies the roto-vibrational excitations of molecules. Due to its wide vibrational frequency range, high spatial and spectral resolution, and operation in the visible or near-infrared range where many organic materials and water are transparent, as opposed to vibrationally resonant infrared spectroscopy [21], Raman spectroscopy has been widely used for microplastics detection. Currently, most studies employed point-confocal Raman spectroscopy, a single-point detection technique. Although this method has exhibited impressive detection capabilities for microplastics and nanoplastics when combined with machine learning algorithms [22], its speed is constrained by the need to scan the sample point by point to obtain the chemical maps. Line-scan Raman spectroscopy is a step in the direction of a fast imaging

technology. It uses a line as excitation, focused to the diffraction limit only in one of the two transversal directions [23–29], so that all points on the line are interrogated at the same time, allowing to increase speed by the number of resolved points along the line, typically by two orders of magnitude. Most of the current research on line-scan Raman imaging technology uses micron-sized plastic beads to verify the imaging performance of the system, but does not apply the technique to micro-plastic detection [30,31].

In this work, we report on a line scan Raman micro-spectroscopy system which realizes rapid imaging and chemical identification of microplastics down to 200 nm size, and can image a 40 μm × 10 μm area in 10s (step size 500 nm, single step exposure time 0.5s), a speed improvement by about two orders of magnitude compared to confocal imaging.

2. Materials and methods

2.1. Confocal line-scan Raman spectroscopy system

A schematics of the confocal line scan Raman tool developed here is shown in Fig. 1. A 532 nm wavelength laser with a TEM00 transversal mode and a power of up to 2 W is used for excitation (Laser Quantum, UK, GEM532). The laser beam is expanded and collimated by the lenses L1 (Thorlabs, USA, ACN127-025-A, f = −25 mm) and L2 (Thorlabs, USA, AC254-125-A, f = 125 mm) to a mode size (at $1/e^2$ intensity) of 4.5 mm. A 532 nm narrow (2.0 nm) bandpass filter NBP (Semrock, USA, LL01-532-12.5) is used to eliminate out of band emission. A concave cylindrical lens CL (Thorlabs, USA, LK1743RM, f = −100 mm) in a far-field (FF) plane of the objective creates a line of beam directions – importantly, by positioning the lens in the FF, a line focus within the objective is avoided, which could damage the objective considering the high laser power. Alternatively, to create a more uniform line intensity, a Powell lens was used as CL, as described later in the text. An achromatic lens L3 (Thorlabs, USA, AC254-100-A, 100 mm) focusses the beam, after reflection by a dichroic mirror DM (Chroma, USA, RT532rdc), into a vertical line in an image plane of the sample (near field (NF)). An achromatic lens L4 (Thorlabs, USA, AC254-200-A, f = 200 mm) acts as tube lens, collimating the beam in horizontal direction towards the infinity corrected objective lens (OBJ), to create an image of the line at the focus plane (NF) of the objective, forming the vertical excitation line on the sample. The FF is the back focal plane of the objective lens, which is conjugated by L3 and L4 to the CL. Different objectives were used, including a long working distance dry (50 × 0.6NA TU Plan ELWD, Nikon, Japan), a high resolution dry (100 × 0.95NA, MPlanApo N, Olympus, Japan) and a water immersion (WI) (40 × 1.15NA, UApo N340, Olympus, Japan) objective. The 9.0 mm beam size at the objective
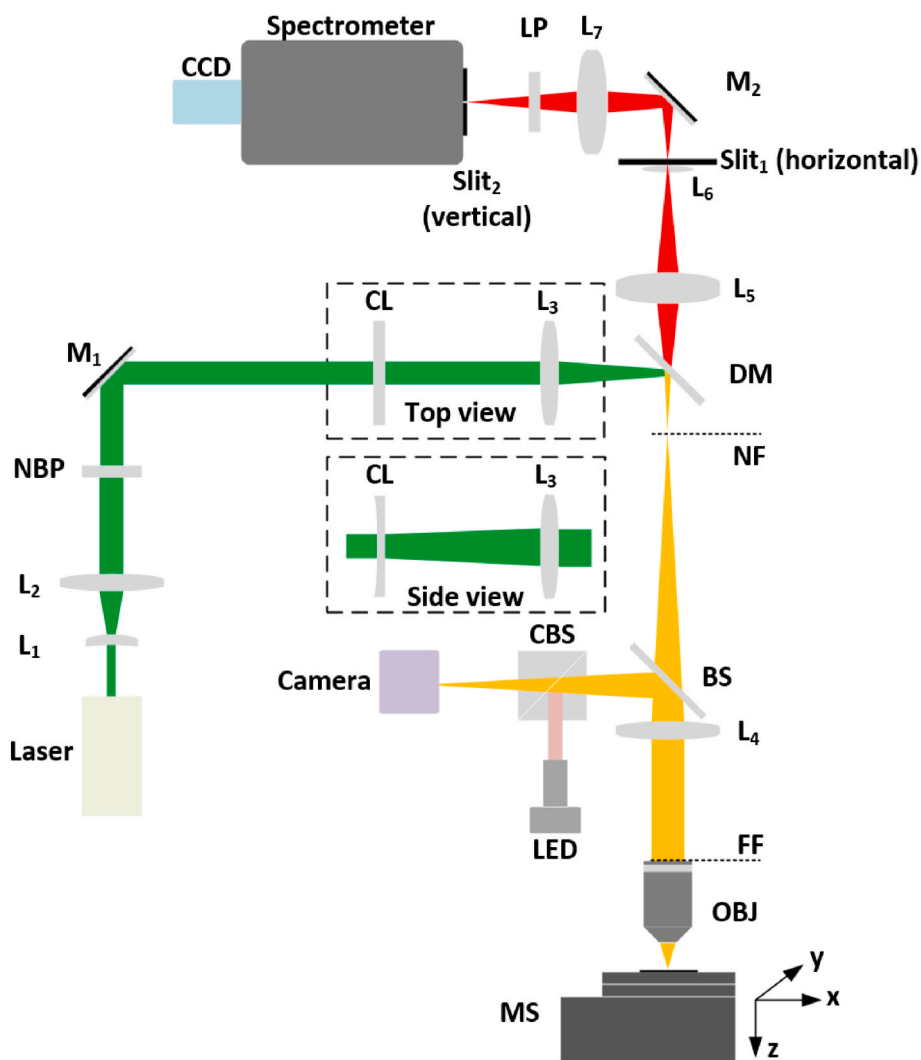

Fig. 1. Sketch of the confocal line-scan Raman spectroscopy setup. L1 to L7 – lenses, NBP - narrow band pass filter, M1 and M2 – mirrors, CL – cylindrical lens, DM – dichroic mirror, BS – beam splitter, CBS – cube beam splitter, OBJ – objective lens, MS – motorized stage, LP – long pass filter, NF – near field image plane, FF – far field image plane.

back focal plane results in a fill factor of 1.88 for the 0.6NA, 2.37 for the 0.95NA, and 0.88 for the 1.15NA objective. The sample was mounted on a custom-built motorized stage (MS) (Jiancheng Optoelectronics, China, X-Y-Z-V05, travel 50 mm, minimal incremental motion 50 nm, maximum speed 3 mm/s) and scanned in the x-y plane. To allow for sample observation by widefield reflection, a removable plate beam splitter BS (Thorlabs, USA, BSX10R, 90:10 R:T) is used to couple in an illumination using an LED module via a cube beam splitter CBS (Thorlabs, USA, CCM1-BS013, 50:50 R:T), and detect the reflected sample image via a camera (Dothinkey, China, M3ST502(M)-H, 3072 × 2048 pixels). The LED module is composed of a white light LED (Thorlabs, USA, MNWHD2, 4900 K), an aspheric condenser lens (Thorlabs, USA, ACL25416U-A, f = 16 mm) and an achromatic lens (Thorlabs, USA, AC254-100-A, f = 100 mm) to form a Köhler illumination.

The Raman scattering and fluorescence of the sample is transmitted through the DM. The signal collection light path uses a dual NF imaging onto two orthogonal slits to allow for confocal selection. L5 and L7 (Edmund, USA, #67–422, f = 50 mm) are Steinheil achromatic triplet lenses which are optimized for 1:1 imaging. Slit1 (Thorlabs, USA, VA100C) is a horizontal confocal slit with adjustable width, controlling the length of the line passing through. Slit2 is a vertical confocal slit which is also the entrance slit of the spectrometer, which provides line-confocality, limiting the detected spatial range across the line, and at the same time controls the spectral resolution. The width of Slit2 is set to 100 μm in our experiments. L6 (Thorlabs, USA, LB1014-A, f = 25 mm) is a biconvex lens mounted on Slit1 to image the FF onto the spectrometer grating to avoid vignetting by the grating, providing equal transmission of the whole line. A pair of long pass filters LP (Semrock, USA, BLP01-532R-25) with a combined optical density of at least 12 at 532 nm between L7 and the spectrometer suppresses laser transmission even for highly reflective sample substrates. They transmit more than 50% above 543 nm, corresponding to Raman scattering with wavenumbers above 380/cm.

The spectrometer is an IsoPlane-320 (Princeton Instruments, USA) with a ruled 600 lines/mm grating (Princeton Instruments, USA, i160-060-500-P, blazed at 500 nm), and the light is detected by a CCD (Princeton Instruments, USA, PIXIS 100B) having a quantum efficiency of about 90% in the range 550–700 nm. It has 1340×100 pixels of 20 μm square size. The gain of the CCD was set to 2 e−/ADU. In the two-dimensional image recorded by the CCD, the vertical dimension maps the vertical dimension of the sample along the excitation line, while the spectrum is dispersed along the horizontal dimension. In this way, a single acquisition provides the spectra for all spatial positions along the excitation line. The 0.6NA dry objective provides a magnification of 50 on the camera, yielding 400 nm per pixel and an imaged height of 40 μm over the 100 pixels used. The 1.15NA WI objective provides a magnification of 44.4 on the camera, yielding 450 nm per pixel, and an imaged height of 45 μm. To obtain a two-dimensional image, the sample is moved orthogonal to the line. Using 2 MHz digitization a full frame is read in 67 ms at a read noise of 11 electrons, while at 100 KHz, 1.34s are needed at 3 electrons read noise. The laser excitation was blocked during readout using a shutter or analog laser power control. For fast scanning, we used 2 MHz and 0.5s integration, allowing to image a 40 μm × 10 μm area with 0.5 μm steps in 10s with the 0.6NA dry objective, which is a two orders of magnitude speed-up compared to confocal imaging.

2.2. Microplastic sample preparation and testing method

We used standard beads (YUAN Biotech, China) and microplastic powder for the investigated samples. The standard beads are either polystyrene (PS) or polymethyl methacrylate (PMMA), with PS bead sizes of 200 nm (YB200), 500 nm (YB500), 1 μm (YB2001), 2 μm (YB2002), and 5 μm (YB2005), and PMMA bead sizes of 1 μm (YBA001), 2 μm (YBA002), and 5 μm (YBA005). The concentration of the stock bead suspension is 25 mg/ml 0.1 ml bead suspension was added to 9.9 ml of a 1:1 v/v water/ethanol solution, providing a bead suspension of

0.25 mg/ml 2 μL of this suspension were pipetted onto a substrate, and allowed to dry in ambient conditions.

We used the PS beads to study the bead size dependence of the imaging. The measurement layout for the two objectives used is shown in Fig. S1. Fused silica substrates (75 × 25 mm) or aluminized glass substrates (75 × 25 mm) were used to reduce substrate fluorescence compared to glass. Aluminized glass substrates were used for 200 nm PS beads. For the dry objectives, the particles were drop-cast on the upper surface of a 1 mm thick substrate, and the laser was focused from air onto this surface. For the WI objective, particles were drop-cast on the lower surface of a 0.17 mm thick substrate, and water was used as immersion medium between the objective and upper substrate surface, allowing the excitation to be focused onto the bottom surface.

For imaging of known heterogeneous samples, we prepared two bead mixtures. The first contains 1 μm PS, 1 μm PMMA, 2 μm PS and 2 μm PMMA in a ratio of 1:1:1:1, and the second contains 5 μm PS and 5 μm PMMA in a ratio of 1:1.

To show the application of the tool to microplastic detection we selected four types of microplastic powders (ShuangFu, China): PS, polyamide (PA), polypropylene (PP) and polyvinyl chloride (PVC). For each powder, a suspension was prepared by mixing 0.1 g powder and 10 mL absolute ethanol, and then the four suspensions were mixed in equal amounts to prepare a mixture suspension, which was drop cast and measured in the same way as the heterogeneous bead solutions above.

2.3. Data processing

2.3.1. Data preprocessing

The Raman data collected by the CCD in the line scan Raman spectroscopy system is a two-dimensional array. The data of each row of pixels of the CCD provides a Raman spectrum. All raw Raman spectroscopy data undergo a preprocessing process of offset subtraction, spectral intensity response correction and background subtraction.

Firstly, the CCD detector offset and dark signal are subtracted from the data, yielding $S_M(\lambda)$. This was done using averaged data taken with the same integration time while blocking the excitation laser.

Then, to correct the non-uniform spectral response, we use a SRM 2242a (National Institute of Standards & Technology) standard material. The shape of the luminescence spectrum of this material is described by an analytical parameterized function [32] $I_{SRM}(\lambda)$, the relative spectral intensity per wavelength. Measuring the luminescence spectrum $S_{SRM}(\lambda)$ of this material, the spectral intensity response correction $F_C(\lambda)$ is determined as $F_C(\lambda) = I_{SRM}(\lambda)/S_{SRM}(\lambda)$. The intensity-corrected Raman spectrum, $S_C(\lambda)$, is then obtained as $S_C(\lambda) = S_M(\lambda)F_C(\lambda)$.

Raman spectra contain luminescence background, which is assumed to be broad and featureless, so that it can be approximately subtracted using a range of methods, including polynomial fitting, wavelet transforms, rolling ball, and many others [33]. We apply here a background subtraction algorithm using a Fourier series as background function and a robust fit method. In this approach, an iterative least squared algorithm is used to fit the data d with a weight w which depends on the sign and amplitude of the residuals,

$$w_j = \begin{cases} 1 & \text{if } d(x_j) \le f(x_j) \\ \exp\left(-\left((d(x_j) - f(x_j))^2 \big/ \sigma^2\right)\right) & \text{else} \end{cases}, \tag{1}$$

where $f(x_j)$ is the value of the fit function at the spectral point x_j. For positive residuals, the Gaussian function suppresses the influence of data with residuals above the noise σ.

The spectrum, defined in the range $x_s \le x \le x_e$, is fitted using the function

$$f(x) = a_0 + \sum_{m=1}^{k} \left[\begin{array}{l} a_i \sin(2\pi m(x - x_s + N\delta)/(2N\delta + x_e - x_s)) + \\ a_{i+k} \cos(2\pi m(x - x_s + N\delta)/(2N\delta + x_e - x_s)) \end{array} \right], \tag{2}$$

where k is the number of Fourier terms included in the fitting function. The Fourier components are defined on a spectral range larger than the data by $2N\delta$, where δ represents the minimum width of the spectral features that will be considered as background, calculated as $(x_e - x_s)/(2(k - N))$. The initial guesses for a_i are estimated by the Fourier coefficients of the spectrum. To ensure the fit converges to the solution closest to the data, we start with a least square fitting with constant weight, and use the resulting residual root mean square r as starting value of σ for the robust fit, which is reduced after each fit according to $\sigma(n) = \overline{\sigma} exp\left(log\left(\frac{r}{\overline{\sigma}}\right)\frac{s-n-1}{s-1}\right)$, with n increasing from 0 to $s - 1$, and $\overline{\sigma}$ the final width, s the number of robust fits to perform. To decrease computational time, we spectrally bin the data with a bin size of 20 for the background fit. For the data shown here we have used $N = 1, k = 3, \overline{\sigma} = 10$ and $s = 5$.

2.3.2. Method of microplastic beads' diameter identification

After taking a line scan Raman image of the bead samples, images of the integrated intensity over relevant Raman peaks were extracted. The apparent size of the beads is determined by the number of pixels above a given threshold, as illustrated in the Supplement Fig. S2. In a simple picture using a laser line width of D, and a bead diameter of d, the distance over which the line is moved covering the entire bead is $D + d$. We use this simple method to determine the approximate diameter of the beads from the Raman image.

2.3.3. Line-scan Raman image data

The data acquired using the line scan Raman spectroscopy system were analyzed using FSC[3] [34–36], an analysis tool which decomposes hyperspectral images into a linear combination of chemical components defined by their non-negative Raman spectra and spatial v/v concentration distributions. This method was previously applied to a range of hyperspectral data including coherent Raman scattering [35], spontaneous Raman [36], and IV-LEEM [37]. Here, the spectra of the microplastics are determined as spatial average in regions corresponding to beads of different chemical composition and used as fixed components in the factorization algorithm, which determines their spatial distribution and the spectrum and concentration of an extra component, which can be identified as the surrounding matrix. The component spectra are normalized so that their spatial concentration maps have unity maximum value.

3. Results and discussion

3.1. Line illumination measurements

The spatial distribution of the combined excitation and detection sensitivity along the line was measured using the 0.6NA objective and a silicon wafer as sample, using the intensity of the silicon Raman peak at 521 cm-1 as homogeneous spatial response.

The line illumination is obtained by the cylindrical lens CL, so that the distribution is given by the laser beam intensity distribution at the CL, which is expected to be close to Gaussian, consistent with the measurements shown in the Supplement Fig. S3, having a $1/e^2$ width of 49 μm.

To create a more uniform intensity, a Powell lens can be used [38] and has been implemented as alternative as follows. The CL was replaced by a Powell lens (Laserline Optics, Canada, LOCP-8.9R05–1.8, fan angle 5°, input beam diameter 1.8 mm), and the beam expander and collimator have been adapted accordingly, using achromatic lenses with focal lengths of 50 mm (Thorlabs, USA, AC254-050-A) as L2 and 60 mm (Thorlabs, USA, AC254-060-A) as L3. A horizontal slit (Thorlabs, USA, VA100C) set to 3 mm height is placed in the NF position to limit the 5.2 mm homogeneous line length created by the Powell lens to a value closer to the imaged height of 2 mm. The resulting line illumination had a uniformity better than 20% as shown in the Supplement Fig. S3. The

Powell lens modification of the setup was used for the 200 nm PS bead and microplastic mixture results, while the cylindrical lens was used for all other data shown.

3.2. Spatial resolution

Results for PS beads of 1 μm and 5 μm size imaged with the 0.6NA objective are shown in Fig. 2. Reflection images are shown in a) and c), while b) and d) are the corresponding Raman intensity images of the 3055-3062 cm^{-1} peak area. The diffraction limited intensity FWHM of a line focus (0.6λ/NA) of the excitation line is 0.53 μm, which is reduced somewhat by the fill factor of the excitation beam. The excitation power was 120 mW at the sample. The stage stepping distance was 200 nm (500 nm) for 1 μm (5 μm) beads, determining the horizontal pixel size of the data. The single step exposure time was 1s. The vertical pixel size is 400 nm. e) and f) show the spectrum at the center of the 1 μm and 5 μm PS bead, respectively.

The observed width of the bead in the Raman intensity is evaluated as the number of pixels over which the intensity is above 20% of the peak intensity, and it is roughly the sum of the line width D and the bead diameter d. In Fig. 2 b), the bead width is 12–14 pixels of 200 nm along the stepping direction. The bead diameter is 5 pixels. The additional 7–9 pixels correspond to 1.4–1.8 μm, this is larger than the diffraction limit due to the spherical shape, probing out of focus regions, and the 20% threshold. For 50% threshold, we find 8 pixels width, close to the diffraction limited resolution. In Fig. 2 d), the bead width is 11–13 pixels of 500 nm along the stepping direction, close to the diameter of the bead of 10 pixels.

Fig. 3 shows the results of 500 nm PS bead using the 0.6NA dry objective. The corresponding results obtained using the 1.15 NA WI objective are given in the Supplement Fig. S4. Fig. 3 a) is the reflection image, and b) is the Raman image of the 3055-3062 cm^{-1} peak area. The excitation power was 180 mW, the single step exposure time was 1s, and the stage step size 100 nm. c) is a zoom of the dashed area in b). The intensity of pixels along the X-axis and Y-axis marked in c) was fitted with a Gaussian of FWHM w and a constant offset. For the 0.6NA dry objective, the FWHM along X-axis and Y-axis are 1052 nm and 659 nm, respectively. For the 1.15NA WI objective, the FWHM along X-axis and Y-axis are 593 nm and 872 nm, respectively. The NA of objective determines the solid angle of Raman scattering collected, scaling approximately with the square of the NA, so that the WI collects about 4 times more than the dry objective, consistent with the higher intensity in the Raman spectrum. The FWHM along the X-axis for the WI objective is smaller than the dry objective, indicating that WI objective lens has a higher resolution in the direction along the scanning direction. The FWHM of X-axis is determined by the scanning accuracy and NA of objective lens, but the FWHM of Y-axis is determined by the single pixel size of CCD and imaging magnification of objective lens, so the FWHM of two axes are different. In our system, the focal length of the tube lens is 200 mm, so the actual magnification of WI objective is 44.4, and the FWHM along Y-axis of WI objective lens is bigger than dry objective due to a too small magnification. The FWHM values are larger than the actual diameter of beads, as they are a convolution of the bead size and the system resolution.

To test the sensitivity of the system to small particles, we measured 200 nm PS beads with the 0.95NA dry objective, as shown in Fig. 4. Aluminum-coated glass substrates were used instead of fused silica substrates to reduce the background and enhance the signal by reflection. Panel a) shows the reflection image of bead – since the diameter of bead is below the diffraction limit, the bead is hardly visible. The excitation power was 24 mW, and the step size 100 nm. Due to the weak Raman signal of the 200 nm bead, which only has 6% of the volume of the 500 nm bead, the single step exposure time was increased to 3 s. Panel b) shows the Raman intensity image of the 3055- 3062 cm^{-1} peak area, in which the bead can be seen and identified as PS using the spectrum at the bead center shown in d). Using FSC[3] analysis, we find a
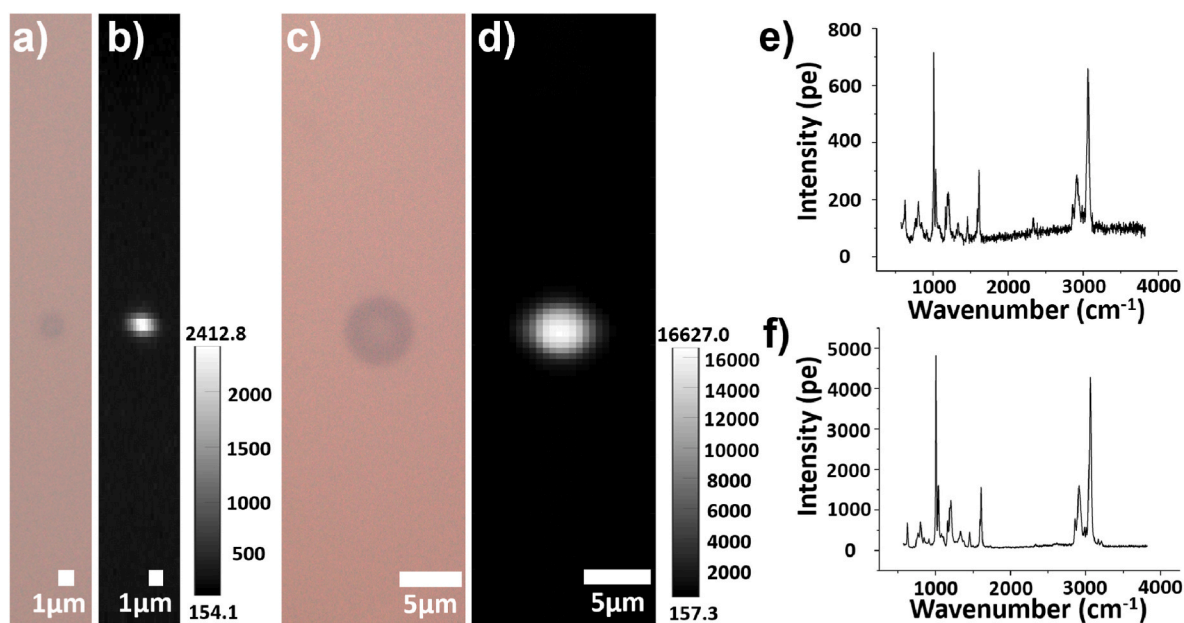
Fig. 2. Spatial imaging of PS beads using the 0.6 NA dry objective. a) Reflection image of a 1 μm bead and b) corresponding line-scan Raman image of the peak area over 3055-3062 cm^{-1} using 200 nm step size. c) and d) - as a) and b) for a 5 μm bead using 500 nm step size. e) and f) spectrum centered at the 1 μm and 5 μm PS bead, respectively. Data were taken with 120 mW at the sample and 1 s exposure time. Gray scale as shown.
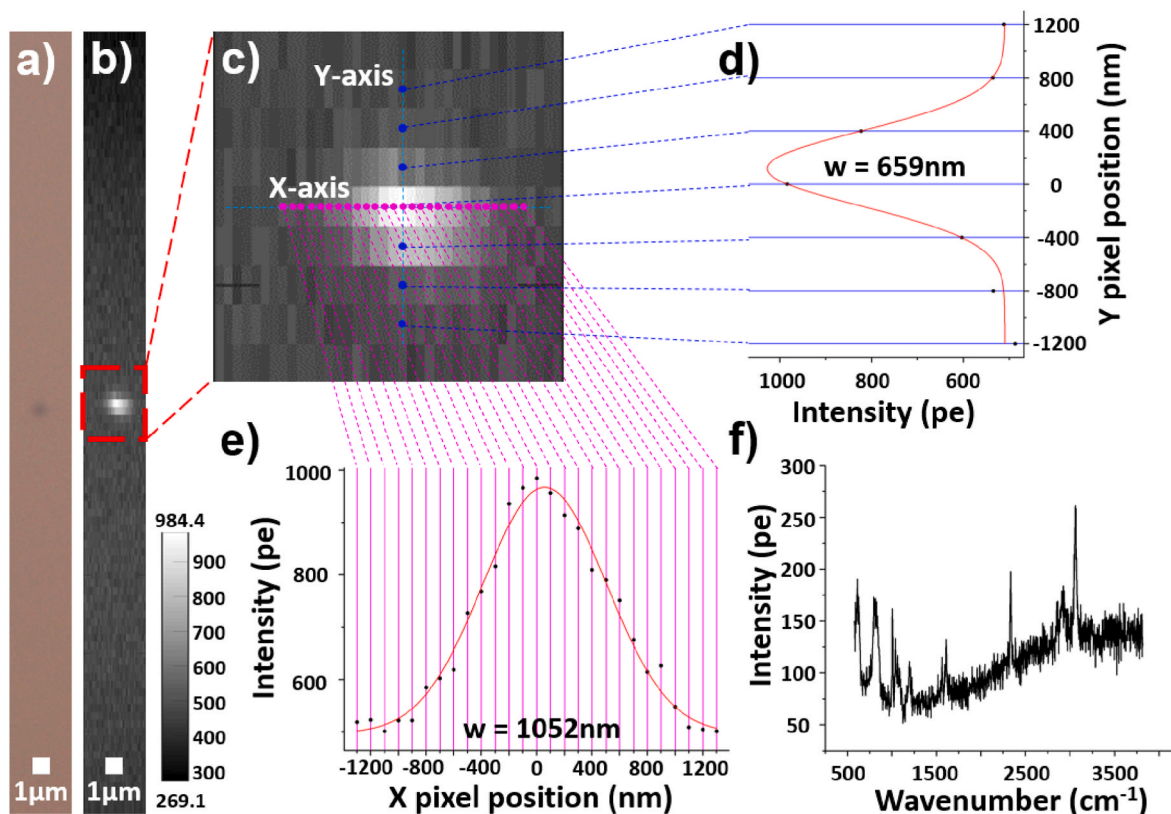

Fig. 3. Raman imaging of a 500 nm PS bead using the 0.6 NA dry objective. a) Reflection image. b) Line scan Raman image of the 3055-3062 cm^{-1} peak area. c) Enlarged image of red dashed line area. d) Gaussian fitting of Raman intensity along vertical (Y) axis. e) Gaussian fitting of Raman intensity along horizontal (X) axis. f) Spectrum at bead center.

PS chemical component with a high signal to noise ratio of 50 of the concentration given in c) and a spectrum shown in e). This demonstrates the exceptional sensitivity of the presented line scan Raman spectroscopy system.

3.3. PS and PMMA bead mixtures

Here we demonstrate chemical imaging on bead mixtures using FSC^3 to separate the components. Results on a 1 μm and 2 μm PS and PMMA
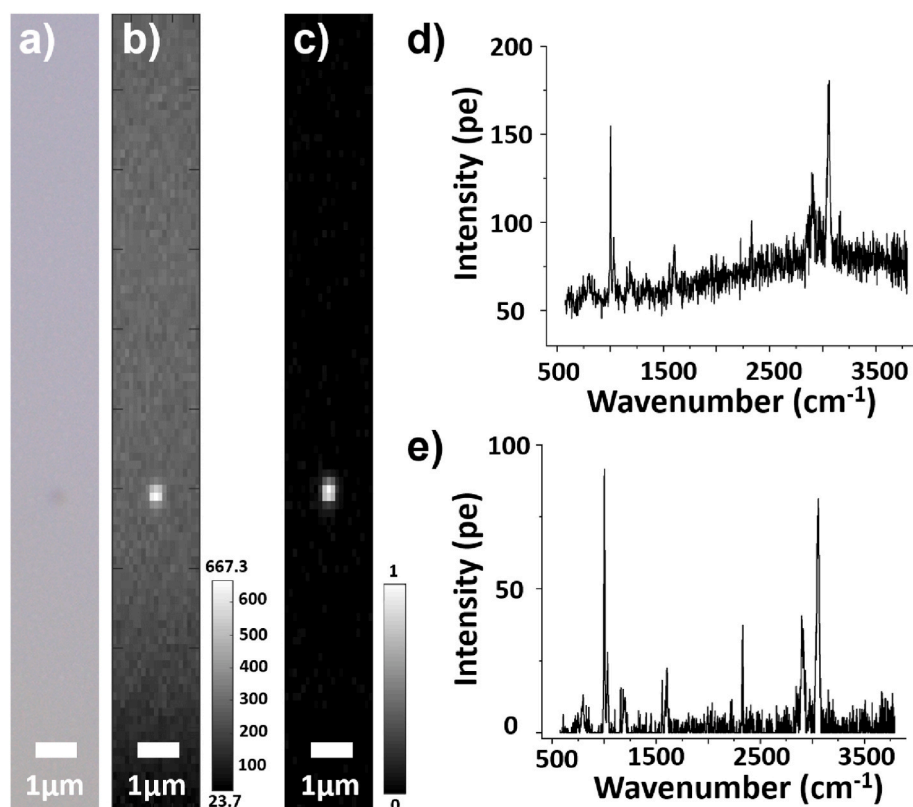
Fig. 4. Results for a 200 nm PS bead using the 0.95NA dry objective. A) Reflection image. B) Line scan Raman image of the 3055- 3062 cm^{-1} peak area. C) PS chemical component concentration image of the region in (a) after FSC^3 analysis. D) Spectrum at bead center. E) PS component spectrum.

bead mixture using the 0.6NA dry objective are given in Fig. 5.

The beads are visible in the reflection image a), and b) shows the corresponding line scan Raman image after FSC^3 analysis, in which red (green) represents the concentration of the PS (PMMA) chemical component. c) shows the component spectra. It can be seen from b) that the line scan image reproduces the spatial position distribution of the beads in a), and for the beads close together, their contours are distinguished. The different bead sizes are visible directly in the shape, but also in the concentration. The diameter of the PS bead (red) in the white circle in Fig. 5 b) is 2 μm, while other beads of weaker signal are 1 μm

diameter. The reduction of the intensity towards the top and bottom edges of the imaged regions by the Gaussian excitation profile is seen in the retrieved concentrations. Specifically, the 1 μm red beads in the central area exhibit higher concentrations compared to those at the edges.

We have also investigated a mixture of 5 μm PS and PMMA beads, with results shown in Supplementary Fig. S5. They are well resolved, and of similar component concentration as all have similar size.
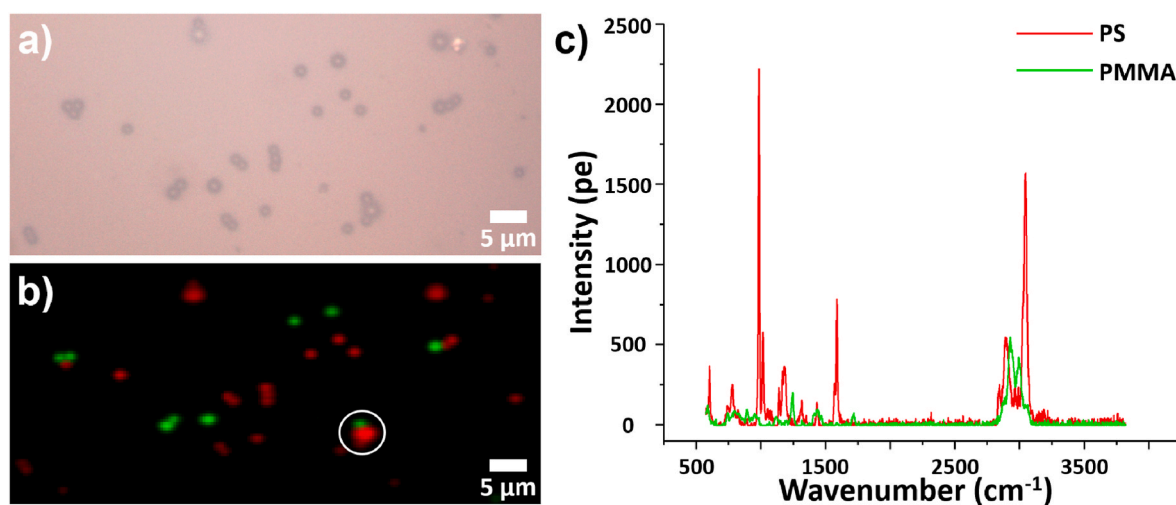

Fig. 5. Results on the 1 μm and 2 μm PS and PMMA bead mixture using the 0.6 NA dry objective. (a) Reflection image. (b) Line scan Raman image of the region in (a) after FSC^3 separating the PS and PMMA chemical components, red: PS concentration, green: PMMA concentration. (c) PMMA and PS component spectra. The excitation power was 120 mW, the single step exposure time was 1 s, and the step size 350 nm.

3.4. Microplastic powder mixture

To show the applicability of the setup to image larger areas exposed to diverse microplastics, we measure mixtures of four types of microplastic powders, PET, PP, PVC, and PMMA using the Powell lens modification and the 0.6NA dry objective. The shapes and sizes of the grains in the powders are highly variable. After drop-casting the sample on the substrate, ethanol evaporates and particles tend to aggregate due to surface tension forces. To image a variety of aggregates and exemplify the speed of the technique we measured a large area of 1.2 mm length and 40 μm height with 240000 pixels, as shown in Fig. 6. The excitation power was 120 mW, the single step exposure time was 0.5 s, and the step size 500 nm, with an imaging time of 20 min. After preprocessing the raw data, we used FSC^3 to decompose it into the chemical components. The component spectra can be attributed to the four types of plastics using known spectra. Fig. 6 a) shows the reflection image of a region on the substrate with the mixture. d)-g) show the component images of PET, PP, PVC and PMMA of the region in a) after FSC^3 analysis, with the brightness corresponding to the square root of the concentration to increase the dynamic range visible. b) shows a color merged image of d)-g). c) is a zoom of the dashed area in b). i) shows a line-cut of the concentration along the red dashed line in g) on a linear scale, to exemplify the dynamic range of the data. h) shows the Raman spectra of different microplastic components after preprocessing, background subtracting and FSC^3 analysis. For clarity, the spectra are offset by 150 pe (photoelectrons) between each spectrum. The irregular shape, the thickness difference of these particles and the unevenness of the surface will affect the Raman intensity. A large range of shapes and structures of various mixed particle aggregates are visible and can be further analyzed to extract particle size statistics for each plastic type.

4. Conclusion

We designed a confocal line scan Raman spectroscopy system and applied it to the detection and identification of microplastic particles. Compared to a point-scanning system, the imaging speed of this system is increased by two orders of magnitude. We use this technology to achieve size identification of microplastic particles, with the ability to detect sizes down to below 200 nm. We employed a Powell lens to create a uniform line illumination and realized rapid imaging and component identification of large areas. The large signal to noise observed in the microplastic data shows that the scan speed could be increased by two orders of magnitude if a camera with a faster readout would be used, such as a CMOS camera, opening the route to the screening of large sample areas. A limitation of Raman imaging is the fluorescence background, which can be overwhelming the Raman signal depending on the sample. However, with a suited data analysis, fluorescence might be identified and used by itself to determine the chemical composition, working in synergy with Raman scattering while using the same instrumentation. The cost of line-scan and confocal Raman imaging systems are comparable, and using machine vision CMOS camera technology has the potential to decrease the cost significantly. With these prospects, line-scan Raman spectroscopy is well placed to analyze real-world environmental samples including the detection and identification of minute plastic particles in complex environmental matrices, offering non-destructive analysis with high sensitivity and high-throughput. By employing appropriate sampling techniques such as filtration or sedimentation, environmental samples from various sources, including water, soil, and air, are accessible.
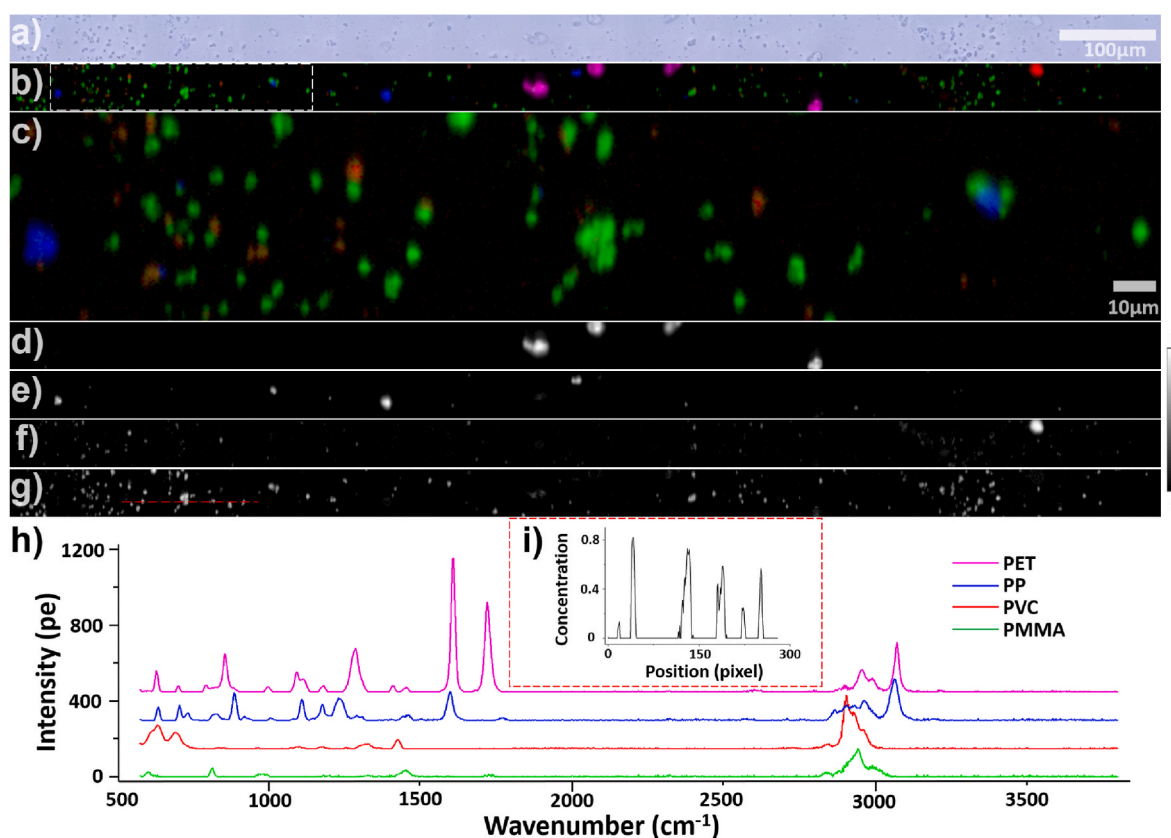

Fig. 6. Large-scale Raman imaging of a powder mixture. a) Reflection image. b) Line scan Raman component concentration image of the region in a) after FSC^3 analysis. Magenta: PET, blue: PP, red: PVC, green: PMMA. c) Enlarged image of white dashed line area in b). d)–g) Separate component concentration images of PET, PP, PVC and PMMA, respectively. h) component spectra, offset for clarity. i) Concentration of PMMA along red dashed line in g).

Credit authors statement

Qingyi Wu: Investigation, Formal analysis, Data curation, Writing – original draft, Writing – review & editing. **Dongyang Xiao**: Investigation. **Nan Wang**: Software, Formal analysis. **Francesco Masia**: Software, Formal analysis. **Wolfgang Langbein**: Conceptualization, Methodology, Software, Writing – review & editing,. **Bei Li**: Conceptualization, Methodology, Funding acquisition.

Declaration of competing interest

The authors declare there are no competing interests.

Data availability

The authors do not have permission to share data.

Appendix A. Supplementary data

Supplementary data to this article can be found online at https://doi.org/10.1016/j.talanta.2023.125067.

References

[1] A. Collignon, J.-H. Hecq, F. Galgani, F. Collard, A. Goffart, Annual variation in neustonic micro-and meso-plastic particles and zooplankton in the Bay of Calvi (Mediterranean–Corsica), Mar. Pollut. Bull. 79 (1–2) (2014) 293–298.

[2] J. Gigault, H. El Hadri, B. Nguyen, B. Grassl, L. Rowenczyk, N. Tufenkji, S. Feng, M. J.N.n. Wiesner, Nanoplastics are neither microplastics nor engineered nanoparticles, Nat. Nanotechnol. 16 (5) (2021) 501–507.

[3] T.S. Galloway, C.N. Lewis, Marine microplastics spell big problems for future generations, Proc. Natl. Acad. Sci. U.S.A. 113 (9) (2016) 2331–2333.

[4] C.-B. Jeong, E.-J. Won, H.-M. Kang, M.-C. Lee, D.-S. Hwang, U.-K. Hwang, B. Zhou, S. Souissi, S.-J. Lee, J.-S. Lee, Microplastic size-dependent toxicity, oxidative stress induction, and p-JNK and p-p38 activation in the monogonont rotifer (Brachionus koreanus), Environ. Sci. Technol. 50 (16) (2016) 8849–8857.

[5] C.D. Rummel, A. Jahnke, E. Gorokhova, D. Kühnel, Schmitt-Jansen, Impacts of biofilm formation on the fate and potential effects of microplastic in the aquatic environment, Environ. Sci. Technol. Lett. 4 (7) (2017) 258–267.

[6] A.J. Watts, M.A. Urbina, R. Goodhead, J. Moger, C. Lewis, T.S. Galloway, Effect of microplastic on the gills of the shore crab Carcinus maenas, Environ. Sci. Technol. 50 (10) (2016) 5364–5369.

[7] J.H. Dekiff, D. Remy, J. Klasmeier, E. Fries, Occurrence and spatial distribution of microplastics in sediments from Norderney, Environ. Pollut. 186 (2014) 248–256.

[8] M. Eriksen, S. Mason, S. Wilson, C. Box, A. Zellers, W. Edwards, H. Farley, S. Amato, Microplastic pollution in the surface waters of the laurentian great lakes, Mar. Pollut. Bull. 77 (1–2) (2013) 177–182.

[9] R.C. Thompson, Y. Olsen, R.P. Mitchell, A. Davis, S.J. Rowland, A.W. John, D. McGonigle, A.E. Russell, Lost at sea: where is all the plastic? Science 304 (5672) (2004), 838-838.

[10] T. Maes, R. Jessop, N. Wellner, K. Haupt, A.G. Mayes, A rapid-screening approach to detect and quantify microplastics based on fluorescent tagging with Nile Red, Sci. Rep. 7 (1) (2017) 1–10.

[11] W.J. Shim, Y.K. Song, S.H. Hong, M. Jang, Identification and quantification of microplastics using Nile Red staining, Mar. Pollut. Bull. 113 (1–2) (2016) 469–476.

[12] D. Fabbri, D. Tartari, C. Trombini, Analysis of poly (vinyl chloride) and other polymers in sediments and suspended matter of a coastal lagoon by pyrolysis-gas chromatography-mass spectrometry, Anal. Chim. Acta 413 (1–2) (2000) 3–11.

[13] D. Fabbri, Use of pyrolysis-gas chromatography/mass spectrometry to study environmental pollution caused by synthetic polymers: a case study: the Ravenna Lagoon, J. Anal. Appl. Pyrolysis 58 (2001) 361–370.

[14] E. Fries, J.H. Dekiff, J. Willmeyer, M.-T. Nuelle, M. Ebert, D. Remy, Identification of polymer types and additives in marine microplastic particles using pyrolysis-GC/MS and scanning electron microscopy, Environ Sci Process Impacts 15 (10) (2013) 1949–1956.

[15] M.-T. Nuelle, J.H. Dekiff, D. Remy, E. Fries, A new analytical approach for monitoring microplastics in marine sediments, Environ. Pollut. 184 (2014) 161–169.

[16] E. Besseling, E. Foekema, J. Van Franeker, M. Leopold, S. Kühn, E.B. Rebolledo, E. Heße, L. Mielke, J. IJzer, P. Kamminga, Microplastic in a macro filter feeder: humpback whale Megaptera novaeangliae, Mar. Pollut. Bull. 95 (1) (2015) 248–252.

[17] Q. Qiu, Z. Tan, J. Wang, J. Peng, M. Li, Z. Zhan, Extraction, enumeration and identification methods for monitoring microplastics in the environment, Estuar. Coast Shelf Sci. 176 (2016) 102–109.

[18] Y.K. Song, S.H. Hong, M. Jang, G.M. Han, M. Rani, J. Lee, W.J. Shim, A comparison of microscopic and spectroscopic identification methods for analysis of microplastics in environmental samples, Mar. Pollut. Bull. 93 (1–2) (2015) 202–209.

[19] Y.K. Song, S.H. Hong, M. Jang, J.-H. Kang, O.Y. Kwon, G.M. Han, W.J. Shim, Large accumulation of micro-sized synthetic polymer particles in the sea surface microlayer, Environ. Sci. Technol. 48 (16) (2014) 9014–9021.

[20] A.S. Tagg, M. Sapp, J.P. Harrison, J,s.J. Ojeda, Identification and quantification of microplastics in wastewater using focal plane array-based reflectance micro-FT-IR imaging, Anal. Chem. 87 (12) (2015) 6032–6040.

[21] P. Ribeiro-Claro, M.M. Nolasco, C. Araújo, Characterization of microplastics by Raman spectroscopy, Compr. Anal. Chem. 75 (2017) 119–151.

[22] C. Fang, Y. Luo, X. Zhang, H. Zhang, A. Nolan, R.J.C. Naidu, Identification and visualisation of microplastics via PCA to decode Raman spectrum matrix towards imaging, Chemosphere 286 (2022), 131736.

[23] J. Xing, S.-H. Kang, Y.-M. Choi, S. Lee, H. Yoo, High-speed line-scan confocal Raman microscope with enhanced diffraction efficiency, Meas. Sci. Technol. 31 (2) (2019), 025203.

[24] J. Ando, A.F. Palonpon, M. Sodeoka, K. Fujita, High-speed Raman imaging of cellular processes, Curr. Opin. Chem. Biol. 33 (2016) 16–24.

[25] K.A. Christensen, M.D. Morris, Hyperspectral Raman microscopic imaging using Powell lens line illumination, Appl. Spectrosc. 52 (9) (1998) 1145–1147.

[26] J. Qin, M.S. Kim, W.F. Schmidt, B.K. Cho, Y. Peng, K. Chao, A line-scan hyperspectral Raman system for spatially offset Raman spectroscopy, J. Raman Spectrosc. 47 (4) (2016) 437–443.

[27] M. Bowden, D.J. Gardiner, G. Rice, D.L. Gerrard, Line-scanned micro Raman spectroscopy using a cooled CCD imaging detector, J. Raman Spectrosc. 21 (1) (1990) 37–41.

[28] L. Kong, P. Zhang, J. Yu, P. Setlow, Y.-q. Li, Rapid confocal Raman imaging using a synchro multifoci-scan scheme for dynamic monitoring of single living cells, Appl. Phys. Lett. 98 (21) (2011), 213703.

[29] K. Watanabe, A.F. Palonpon, N.I. Smith, L.-d. Chiu, A. Kasai, H. Hashimoto, S. Kawata, K. Fujita, Structured line illumination Raman microscopy, Nat. Commun. 6 (1) (2015), 10095.

[30] K. Mochizuki, Y. Kumamoto, K. Fujita, Multiline Illumination Raman Microscopy for Rapid Cell Imaging, Biomedical Imaging and Sensing Conference 2020, International Society for Optics and Photonics, 2020, p. 115210F.

[31] J. Qi, W.-C. Shih, Performance of line-scan Raman microscopy for high-throughput chemical imaging of cell population, Appl. Opt. 53 (13) (2014) 2881–2885.

[32] N.I.o.S. Technology, Certificate - Standard Reference Material 2242a (2019).

[33] K.H. Liland, T. Almøy, B.-H. Mevik, Optimal choice of baseline correction for multivariate calibration of spectra, Appl. Spectrosc. 64 (9) (2010) 1007–1016.

[34] F. Masia, P. Borri, W. Langbein, Sparse sampling for fast hyperspectral coherent anti-Stokes Raman scattering imaging, Opt Express 22 (4) (2014) 4021–4028.

[35] F. Masia, A. Glen, P. Stephens, P. Borri, W. Langbein, Quantitative chemical imaging and unsupervised analysis using hyperspectral coherent anti-Stokes Raman scattering microscopy, Anal. Chem. 85 (22) (2013) 10820–10828.

[36] F. Masia, A. Karuna, P. Borri, W. Langbein, Hyperspectral image analysis for CARS, SRS, and Raman data, J. Raman Spectrosc. 46 (8) (2015) 727–734.

[37] F. Masia, W. Langbein, S. Fischer, J.-O. Krisponeit, J. Falta, Low-energy electron microscopy intensity–voltage data – factorization, sparse sampling and classification, J. Microsc. (2022) 1–16, 00.

[38] I. Powell, Design of a laser beam line expander, Appl. Opt. 26 (17) (1987) 3705–3709.